Mathematics

AIMS Mathematics, 8(7): 15805–15823.
DOI: 10.3934/math.2023807
Received: 22 March 2023
Revised: 18 April 2023
Accepted: 19 April 2023
Published: 04 May 2023

http://www.aimspress.com/journal/Math

Research article

Neural networking analysis for MHD mixed convection Casson flow past a multiple surfaces: A numerical solution

Khalil Ur Rehman[1,2,*], Wasfi Shatanawi[1,3,4,*], Zeeshan Asghar[1,5] and Haitham M. S. Bahaidarah[6,7]

[1] Department of Mathematics and Sciences, College of Humanities and Sciences, Prince Sultan University, Riyadh 11586, Saudi Arabia
[2] Department of Mathematics, Air University, PAF Complex E-9, Islamabad 44000, Pakistan
[3] Department of Medical Research, China Medical University Hospital, China Medical University, Taichung, 40402, Taiwan
[4] Department of Mathematics, Faculty of Science, The Hashemite University, P.O. Box 330127, Zarqa 13133, Jordan
[5] NUTECH, School of Applied Sciences and Humanities, National University of Technology, Islamabad, 44000, Pakistan.
[6] Department of Mechanical Engineering, King Fahd University of Petroleum and Minerals, Dhahran 31261, Saudi Arabia
[7] Interdisciplinary Research Center for Renewable Energy and Power Systems, King Fahd University of Petroleum and Minerals, Dhahran 31261, Saudi Arabia

* **Correspondence:** Email: kurrehman@psu.edu.sa, wshatanawi@psu.edu.sa.

Abstract: The heat and mass transfer within non-Newtonian fluid flow results in complex mathematical equations and solution in this regard remains a challenging task for researchers. The present paper offers a numerical solution for the non-Newtonian flow field by using Artificial neural networking (ANN) model with the Levenberg Marquardt training technique. To be more specific, we considered thermally magnetized non-Newtonian flow headed for inclined heated surfaces. The flow is carried with viscous dissipation, stagnation point, heat generation, mixed convection, and thermal radiation effects. The concentration aspects are entertained by the owing concentration equation. The shooting method is used to solve the mathematical flow equations. The quantity of interest includes the temperature and heat transfer coefficient. Two different artificial neural networking models have been built. The training of networks is done by use of the Levenberg Marquardt technique. The values

of the coefficient of determination suggest artificial neural networks as the best method for predicting the Nusselt number at both surfaces. The thermal radiation parameter and Prandtl number admit a direct relationship to the Nusselt number while the differing is the case for variable thermal conductivity and Casson parameters. Further, by using Nusselt number (NN)-ANN models, we found that for cylindrical surface, the strength of the NN is greater than the flat surface.

Keywords: neural networking; Levenberg-Marquardt algorithm; shooting method; heat transfer; thermal radiations; mixed convection
Mathematics Subject Classification: 35A25, 65MO6, 76D05

1. Introduction

Non-Newtonian fluids are used in a variety of products, including culinary items, personal protective equipment, printing technologies, damping and braking systems, and drag-reducing agents [1]. Fluids that are not Newtonian exhibit complex rheological behavior [2]. Unlike Newtonian fluids, these materials do not behave linearly between the shear rate or shear and viscosity. Non-Newtonian fluids [3,4] are categorized into many groups based on how they react to changes in shear stress or rate. Based on their behavior, non-Newtonian fluids can be classified as shear thinning [5,6], shear thickening [7,8], thixotropic, visco-plastic, and rheopectic fluids. Following such characteristics, various studies were given by researchers to explore the type of non-Newtonian fluid models and the corresponding daily life applications. In this direction, the Casson fluid model is one of the non-Newtonian fluid models that best capture yield stress and has noteworthy applications in the biomechanics and polymer sectors. Several different goods, including synthetic lubricants, medicinal compounds, paints, coal, china clay, and many others, can be prepared using Casson fluid. Human blood can also be referred to as Casson fluid since it contains a variety of components including human red blood cells, fibrinogen, protein, and globulin in aqueous base plasma. The operative use of Casson fluid in biological treatments, drilling processes, bio-engineering and food processing has captured the attention of researchers like the analysis of diffusion phenomena in stenosed capillary-tissue exchange systems provided by Siddiqui and Mishra [9]. In order to depict the blood flow they utilize a modified Casson's fluid description. Through the alteration of a measure known as the retention parameter, the severity of the condition could be evaluated. Another significant aspect of this analysis was the increase of these variables together with the progression of the stenosis. For the investigation of the normal and sick states, the concentration profiles were identified. In the recent past, according to Abolbashari et al. [10], engineering and industrial applications have found usage for nano-fluids because of their fantastic thermal conductivity increase. Due to their significance, analyze the fluid non-Newtonian flow with nanoparticles towards the sheet. In special circumstances, the current analytical solution shows a very strong correlation with those of the earlier research that was published. The impact of various flow physical factors were thoroughly explored. Bhattacharyya et al. [11] conducted an examination of Casson fluid flow past a shrinking surface with different effects. Self-similar nonlinear ordinary differential equations (ODEs) were obtained. The translated energy and velocity equations both had two exact answers. According to the depicted data, the temperature drops for greater values of radiation parameter, Prandtl number, and power-law exponent. Additionally, the thickness of the thermal boundary layer increases with direct variation in wall temperature. In some instances, temperature

overshoot was seen in the temperature field's graphical depiction. Therefore, under some circumstances, heat transfer from the surface happens instead of heat absorption at the surface. In the presence of fluctuating suction, Abd El-Aziz and Yahya [12] investigated the impact of Hall current on the Casson fluid flow over a sheet. To obtain non-dimensional flow fields, the resulting equations were analytically solved. The temperature and velocity profiles are studied for various parameter values that entered the problem and were displayed graphically. Physically relevant Nusselt number was sorted out and displayed as graphics. For an axisymmetric Casson stagnation point, Nawaz et al. [13] looked at the effects of Joule heating and viscous dissipation. The ensuing boundary value issue was resolved using the homotopy analysis method. The homotopy solutions and the numerical outcomes were compared. The behavior of various parameters was examined. The Casson fluid parameter's resultant effect seems to accelerate the fluid's velocity. The actions of dissipation and Joule heating cause the system to warm up. The thermal and velocity slip effects on a Magnetohydrodynamics (MHD) Casson fluid were studied by Usman et al. [14] over a cylinder with Buongiorno's model. The Casson nanofluid model's equations were constructed and reduced by using similarity transformation. The collocation approach was used to arrive at the numerical solution. The graphs that compare the nanofluid fluid flow to the emerging physical parameters provide an analysis of the physical quantities of interest. The effects of Newtonian heating on the Casson fluid flow were examined by Tassaddiq et al. [15]. In this study, porous effects for such fluids and MHD effects were also taken into account. Equations involving partial differentials were used to model the fundamental issue. The analytical tool is known as the Laplace transform was used to achieve the "Velocity" and "Temperature" functions. In order to analyze the modeling parameters that were used, graphical representations were used. To verify the facts, numerical calculations were made. The graphical results show that velocity clearly declines for magnetic parameter is intensified and increases as the porosity parameter is increased (conjugate parameter). For all conceivable Casson parameter values, the fluid flow might be controlled. A comparative examination of multiphase flow over a steep channel was carried out by Hussain et al. [16]. The combination of microscopic gold particles with Casson fluid creates an intuitive non-Newtonian particulate suspension. Consideration of a uniformly slanted conduit allowed for the consideration of gravitational and magnetic influences. The shear-thinning phenomena is further influenced by heating effects at the channel's edge. For two-phase fluid flow with heat transfer, an exaction was found. In addition, Newtonian-gold particulate flow and Casson-gold particulate flow, which was a non-Newtonian suspension of particle flow, are contrasted. It was discovered that the shear-thinning effects of magnetized Newtonian particle suspension across the inclined channel are more pronounced and experience reduced skin friction. However, it was discovered that Casson fluid was a very helpful suspension for the fabrication and coatings processes, among other things. Additionally, the magnetic field affects the mobility of both phases as a resistive force. Due to the system's significant viscous dissipation, more energy was added. Akolade and Tijani [17] discussed the effect of various transport parameters on Casson- nanofluids through a Riga surface. After imposing sufficient similarity factors, the flow equations were derived. To account for all relevant flow characteristics, the spectral quasi-linearization technique (SQLM) was used. Aside from great agreement with previously published work, the approach performance (numerical estimation tools) was examined in terms of CPU time and mistakes. For the current challenge, engineering dimensionless parameters were also supplied. The outcomes demonstrated that the Casson fluid had a lower flow resistance than the Williamson fluid. Furthermore, Casson fluid diffuses and conducts less than Williamson fluid. Siddiqui et al. [18] investigated the Casson nanofluid between two spinning and stretchy disks in this study. The effects

of thermal radiation, magnetic field, Darcy Forchheimer flow, and heat source were investigated. The shooting strategy was owned to solve the existing equations with the help of MATLAB packages. The temperature profile when the Prandtl number was varied was also discussed. Furthermore, the thermal profile towards the thermophoresis, radiation, and Brownian parameter was investigated. Graphs were used to evaluate the impact of nanoparticle concentration on microorganisms with rising Peclet and Lewis numbers. References [19–22] provide an evaluation of the most recent attempts at Casson fluid flow in a variety of configurations.

In this paper, we used the prediction application of artificial intelligence to examine the thermal stagnation point magnetized flow field of non-Newtonian fluid flow due to inclined heated stretched surfaces with thermos-physical effects namely viscous dissipation, mixed convection, heat generation, and variable thermal conductivity. The flow is mathematically formulated for a cylindrical surface and later mathematical reduction is done for thermal flow over a flat surface. The ultimate results are obtained by using the shooting method and are offered as line graphs. The quantity of interest includes the temperature and NN at both flat and cylindrical surfaces. Two different ANN models are constructed to forecast the heat transfer coefficient at surfaces. We are confident that the thermal findings by the use of ANN models will helpful for investigators affiliated with the area of thermal engineering.

2. Flow formulation

Stretching inclined surfaces, such as the cylinder and plate, are used to introduce non-Newtonian fluid flow. By taking into account the magnetic field [23–25], mixed convection, stagnation point flow [26], temperature-dependent conductivity [27], viscous dissipation [28], and heat generation [29] the novelty of the flow field is strengthened. By utilizing the concentration equation, the mass transfer is taken into account. It is assumed that the strength of temperature and concentration is considered higher at surfaces in comparison with strength far away from the surface. The concluding Casson fluid flow equations [26] for the given problem are expressed as

$$\frac{\partial(\hat{r}\hat{u})}{\partial\hat{x}} + \frac{\partial(\hat{r}\hat{v})}{\partial\hat{r}} = 0, \tag{1}$$

$$\hat{u}\frac{\partial\hat{u}}{\partial\hat{x}} + \hat{v}\frac{\partial\hat{u}}{\partial\hat{r}} = \nu\left(1+\frac{1}{\beta}\right)\left(\frac{\partial^2\hat{u}}{\partial\hat{r}^2} + \frac{1}{\hat{r}}\frac{\partial\hat{u}}{\partial\hat{r}}\right) + \hat{u}_e\frac{\hat{u}_e}{\partial\hat{x}} - \frac{\sigma {B_0}^2}{\rho}(\hat{u}-\hat{u}_e)$$
$$+ g_0(\hat{T}-\hat{T}_\infty)B_T\,cos(\alpha) + g_0(\hat{C}-\hat{C}_\infty)B_C\,cos(\alpha), \tag{2}$$

$$\rho c_\rho\left(\hat{u}\frac{\partial\hat{T}}{\partial\hat{x}} + \hat{v}\frac{\partial\hat{T}}{\partial\hat{r}}\right) = \frac{1}{\hat{r}}\frac{\partial}{\partial\hat{r}}\left(\kappa\frac{\partial\hat{T}}{\partial\hat{r}}\right) + \bar{\mu}\left(1+\frac{1}{\beta}\right)\left(\frac{\partial\hat{u}}{\partial\hat{r}}\right)^2 - \frac{1}{\hat{r}}\frac{\partial}{\partial\hat{r}}(\hat{r}\hat{q}) + Q_0\left(\hat{T}-\hat{T}_\infty\right). \tag{3}$$

$$\hat{u}\frac{\partial\hat{C}}{\partial\hat{x}} + \hat{v}\frac{\partial\hat{C}}{\partial\hat{r}} = D_m\frac{\partial^2\hat{C}}{\partial\hat{r}^2}. \tag{4}$$

The radioactive flux and thermal conductivity relations are given as:

$$\hat{q} = -\frac{16\sigma^*T_\infty^3}{3k^*}\frac{\partial\hat{T}}{\partial\hat{r}},$$

$$\kappa(\hat{T}) = \kappa_\infty\left(1+\varepsilon\frac{\hat{T}-\hat{T}_\infty}{\hat{T}_w-\hat{T}_\infty}\right), \tag{5}$$

The flow conditions are:

$$\hat{u} = \hat{U}_w = a\hat{x},, \hat{C} = \hat{C}_w, \hat{v} = 0\hat{T} = \hat{T}_w, \text{ at } \hat{r} = R_c,$$
$$\hat{u} = \hat{u}_e = d\hat{x}, \hat{C} \to \hat{C}_\infty, \hat{T} \to \hat{T}_\infty, \text{ as } \tilde{r} \to \infty. \quad (6)$$

Here, ν is kinematic viscosity, R_c stands for radius of cylinder, B_T is the thermal expansion coefficient,B_C denote the coefficient of solutal expansion, $\rho, \hat{T}, \hat{C}, Q_0, \varepsilon, \kappa_\infty$and D_m are fluid density, temperature, concentration, heat generation coefficient, small parameter, heat conductivity far from the surface and mass diffusivity respectively. By using NN-ANN model, we are interested in comparing how flow parameters affect the Nusselt number and temperature of Casson fluid flow toward both surfaces. Consequently, we must convert these partial differential equations (PDEs) into corresponding ODEs in order to solve Eq (1) through (4). For this reason, we have own the following set of variables [26,27]:

$$\eta = \frac{\hat{r}^2 - {R_c}^2}{2R_c}\sqrt{\frac{U_0}{\nu L}}, \hat{u} = \hat{x}\frac{U_0}{L}F'(\eta), \ \hat{v} = -\frac{R_c}{\hat{r}}\sqrt{\frac{\nu U_0}{L}}F(\eta),$$

$$\phi_n(\eta) = \frac{\hat{C}-\hat{C}_\infty}{\hat{C}_w-\hat{C}_\infty}, \theta_n(\eta) = \frac{\hat{T}-\hat{T}_\infty}{\hat{T}_w-\hat{T}_\infty}. \quad (7)$$

Owning Eq (7), Eqs (1)–(3) turns into

$$\left(F'''(1+2\gamma_p\eta)+2\gamma_p F''\right)\left(1+1/\beta_p\right) + FF'' - F'^2 + G_T\theta_n\cos(\alpha) + G_C\phi_n\cos(\alpha)$$
$$-{M_p}^2(F'-A_p) + {A_p}^2 = 0, \quad (8)$$

$$\left(\theta_n''(1+2\gamma_p\eta)+2\gamma_p\theta_n'\right)\left(1+\frac{4}{3}R_p\right) + \varepsilon_T\left((\theta_n'^2+\theta_n\theta_n'')(1+2\eta\gamma_p)+2\theta_n\gamma_p\theta_n'\right)$$
$$+ Pr\,E_n\left(1+2\eta\gamma_p\right)F''^2\left(1+\frac{1}{\beta_p}\right) + Pr\,H_p\,\theta + Pr\,\theta_n'F = 0, \quad (9)$$

$$\phi_n''(1+2\eta\gamma_p) + 2\gamma_p\phi_n' + ScF\phi_n' = 0. \quad (10)$$

and flow conditions reduced as:

$$F' = 1, F = 0, \theta_n = 1, \phi_n = 1, \text{at}\eta = 0,$$
$$F' = A_p, \theta_n = 0, \phi_n = 0, \text{at}\eta \to \infty. \quad (11)$$

The parameters are given as:

$$\beta_p = \frac{\bar{\mu}\sqrt{2\pi_c}}{\tau_r}, \ R_p = \frac{4\sigma^*\tilde{T}_\infty^3}{\kappa k^*}, \ \gamma_p = \sqrt{\frac{\upsilon L}{c^2U_0}},$$

$$A_p = \frac{d}{a}, M_p = \sqrt{\frac{\sigma B_0^2 L}{\rho U_0}}, \ Pr = \frac{\bar{\mu}c_p}{\kappa}, \ E_n = \frac{U_0^2(\hat{x}/L)^2}{c_p(\hat{T}_w-\hat{T}_\infty)}, \ G_T = \frac{g_0\beta_T(\hat{T}_w-\hat{T}_\infty)L^2}{U_0\hat{x}}, G_C =$$
$$\frac{g_0\beta_C(\hat{C}_w-\hat{C}_\infty)L^2}{U_0\hat{x}}, Sc = \frac{\nu}{D_m}, H_p = \frac{LQ_0}{U_0\rho c_p}. \quad (12)$$

The Casson fluid parameter, Prandtl number, Eckert number, thermal radiation parameter, Solutal Grashof number, thermal Grashof number, velocities ratio parameter, and Schmidt number are symbolized by $\beta_p, Pr, E_n, R_p, G_C, G_T, A_p$ and Sc. The heat transfer at inclined surfaces is considered a key physical effect and to evaluate heat transfer we considered the Nusselt number. The mathematical relationship [26] of NN is:

$$\left.\begin{aligned} &Nu_{\hat{x}} = \frac{\hat{x}q_w}{\kappa(\hat{T}_w - \hat{T}_\infty)}, q_w = -\kappa\left(1 + \frac{16\sigma^*\hat{T}_\infty^3}{3k^*\kappa}\right)\left(\frac{\partial\hat{T}}{\partial\hat{r}}\right)_{\hat{r}=R_c}, \\ &\frac{Nu_{\hat{x}}}{\sqrt{Re_{\hat{x}}}} = -\left(1 + \frac{4}{3}R_p\right)\theta_n'(0) \end{aligned}\right\}. \tag{13}$$

3. Numerical scheme

The lower order equations, Eqs (8)–(10), can be used to examine the non-Newtonian fluid flow regime. Due to their coupling and nonlinearity, they are challenging to solve analytically. The flow differential equations are reported using a number of various solution approaches [30–35], however, the shooting method will be employed to get numerical solution for the present research problem. The name of the shooting technique is taken from an analogy with target shooting: we shoot at the target and watch where it lands; based on the misses, we can modify our aim and shoot again in the hopes that it would hit close to the target. To convert boundary value problems into similar initial value problems, the shooting method was developed. The supportive material in this regard can be accessed in Refs. [25–27]. Having an initial value system is a vital first step in this regard. We can achieve it by presuming:

$$\begin{aligned} Y_1 = F(\eta), Y_2 = F'(\eta), Y_3 = F''(\eta), \\ Y_4 = \theta_n(\eta), Y_5 = \theta_n'(\eta), \\ Y_6 = \phi_n(\eta), Y_7 = \phi_n'(\eta), \end{aligned} \tag{14}$$

under Eq (14), Eqs (8)–(10) reduces to

$$\begin{aligned} Y_1' &= Y_2, \\ Y_2' &= Y_3, \\ Y_3' &= \frac{1}{\left(1 + \frac{1}{\beta_p}\right)(1 + 2\eta\gamma_p)}\begin{bmatrix} -2\gamma_p Y_3\left(1 + \frac{1}{\beta_p}\right) + Y_2^2 - Y_1 Y_3 - G_T Y_4 \cos\alpha - G_C Y_6 \cos\alpha \\ -M_p{}^2(Y_2 - A_p) - A_p{}^2 \end{bmatrix}, \\ Y_4' &= Y_5, \\ Y_5' &= -\frac{1}{\left(1 + \frac{4}{3}R_p\right)(1 + 2\eta\gamma_p) + \varepsilon_T(1 + 2\eta\gamma_p Y_4}\begin{bmatrix} (1 + \frac{4}{3}R_p)(2\gamma_p Y_5) + \varepsilon_T((1 + 2\eta\gamma_p)Y_5^2 \\ +2\gamma_p Y_4 Y_5) + Pr\, Y_1\, Y_5 + Pr\, H_p\, Y_4 \\ + Pr\, E_n\,(1 + 2\eta\gamma_p)(1 + \frac{1}{\beta_p})Y_3^2 \end{bmatrix} \\ Y_6' &= Y_7, \\ Y_7' &= \frac{-ScY_1Y_6 - 2\gamma_p Y_7}{(1 + 2\eta\gamma_p)}. \end{aligned} \tag{15}$$

The flow equations turns down to:

$$Y_1 = 0, Y_2 = 1, Y_6 = 1, Y_4 = 1, \text{at} \eta = 0,$$
$$Y_2 \to A_p, Y_6 \to 0, Y_4 \to 0, \text{as} \eta = \infty. \tag{16}$$

The self-coding scheme of shooting is carried out in Matlab for the present problem and outcomes are shared in terms of graphs and numerical data.

4. Artificial neural networking model

Mathematical modeling is done for the Casson flow over heated stretched surfaces. The equations for non-Newtonian flow are numerically solved. Both a flat plate and a cylindrical surface are used to evaluate the Nusselt number. The Nusselt number at surfaces is predicted using ANN models in both situations. Researchers firmly think that the multilayer perceptron (MLP) and ANN model [36–40] have excellent learning capabilities and can be utilized to anticipate a variety of physical occurrences. In MLP networks, three separate layers are utilized. The first layer uses the inputs, while the centrally important layer is referred to as the hidden layer. The output layer, which is the final layer, is where the prediction data is stored. The NN-ANN-I and II are two ANN models that we have created. Whereas NN-ANN-II is designed to provide predictions of Nusselt number values at cylindrical surfaces, NN-ANN-I is built to forecast the Nusselt number at flat surfaces. The five parameters are employed as inputs and the NN is taken into account as an output for both NN-ANN models. Variable thermal conductivity, heat generation, Prandtl number, the Casson fluid, and the thermal radiation parameters are the flow parameters.

Table 1 provides the symbolic information for models. Network architecture is given in Figure 1. We have gathered 80 samples for the five inputs, leading to 80 sample values for the Nusselt number. 15% of the data is used for validation while the remaining 70% is used to train the network. Testing also makes advantage of the 15%. Table 2 provides all available details in this regard. Ten (10) neurons are taken into account in the hidden layer, and the network is trained using the Levenberg-Marquardt method. The transfer functions used in hidden and output have the following expressions:

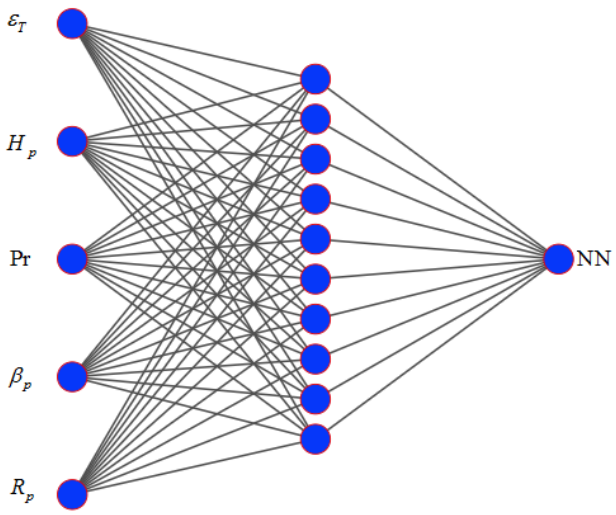

Figure 1. Architecture of ANN.

Table 1. Neural networking detail.

Model	Surface	Input					Output
NN-ANN Model-I	$(\gamma_{p=}0.0)$	(ε_T)	(H_p)	(Pr)	(β_p)	(R_p)	NN
NN-ANN Model-II	$(\gamma_{p=}0.5)$	(ε_T)	(H_p)	(Pr)	(β_p)	(R_p)	NN

Table 2. Description of NN data.

Samples	NN-ANN Model-I	NN-ANN Model-II
Total samples	80	80
Training	56	56
Validation	12	12
Testing	12	12

$$F_T(x) = \frac{1}{1+e^{-x}}, \tag{17}$$

$$\text{Pureline}(x)=x. \tag{18}$$

We have taken into consideration the mean squared error (MSE) and coefficient of determination (R) for performance analysis of ANN models. The mathematical formulas are expressed as:

$$MSE = \frac{1}{N}\sum_{i=1}^{N}(X_{\text{num}(i)} - X_{\text{ANN}(i)})^2. \tag{19}$$

$$R = \sqrt{1 - \frac{\sum_{i=1}^{N}(X_{\text{num}(i)} - X_{\text{ANN}(i)})^2}{\sum_{i=1}^{N}(X_{\text{num}(i)})^2}}. \tag{20}$$

5. Results and discussion

Using ANN models, the Casson flow toward two distinct heated surfaces is studied. The heat transfer coefficient and Casson fluid temperature are included in the quantity of interest. A mathematical formulation and shooting method is used to solve flow equations.

By taking the curvature parameter's zero value into consideration, the Casson fluid flow over a flat surface is assessed. The most important flow parameters for studying the flow field are the thermal radiation parameter, Prandt number, heat generation parameter, and variable thermal conductivity. We have assessed these parameters' effects on the NN at flat and cylindrical surfaces see Tables 3–10. Table 3 shows the variation in the NN in the presence of positive values for the variable thermal conductivity parameter. Both plates and cylinders are subject to this kind of inspection. The heat transfer normal to the surface is measured as a Nusselt number. The NN is seen to decrease for variations in the variable thermal conductivity parameter. For cylindrical surfaces, the Nusselt number is larger in magnitude. Table 4 shows the influence of a varied thermal conductivity parameter on the NN in the absence of heat generation.

Table 3. Impact of ε_T on NN.

	$\boldsymbol{\theta_n'(0)}$		$\boldsymbol{-(1+4/3R_p)}$	
$\boldsymbol{\varepsilon_T}$	$\gamma_p = 0$ (Plate)	$\gamma_p = 0.5$(Cylinder)	$\gamma_p = 0$ (Plate)	$\gamma_p = 0.5$ (Cylinder)
0.1	−0.3868	−0.5200	0.5415	0.7280
0.2	−0.3782	−0.5152	0.5295	0.7213
0.3	−0.3702	−0.5107	0.5183	0.7150
0.4	−0.3625	−0.5064	0.5075	0.7090
0.5	−0.3553	−0.5023	0.4974	0.7032
0.6	−0.3484	−0.4985	0.4878	0.6979
0.7	−0.3419	−0.4947	0.4787	0.6926
0.8	−0.3357	−0.4912	0.4700	0.6877
0.9	−0.3298	−0.4877	0.4617	0.6828
1.0	−0.3187	−0.4813	0.4462	0.6738

Table 4. Impact of $\varepsilon_T$on NN when $H_p = 0$.

	$\boldsymbol{\theta_n'(0)}$		$\boldsymbol{-(1+4/3R_p)}$	
$\boldsymbol{\varepsilon_T}$	$\gamma_p = 0$ (Plate)	$\gamma_p = 0.5$(Cylinder)	$\gamma_p = 0$ (Plate)	$\gamma_p = 0.5$ (Cylinder)
0.1	−1.3699	−0.9213	1.9179	1.2898
0.2	−1.3414	−0.9107	1.8780	1.2750
0.3	−1.3145	−0.9005	1.8403	1.2607
0.4	−1.2890	−0.8908	1.8046	1.2471
0.5	−1.2649	−0.8815	1.7709	1.2341
0.6	−1.2420	−0.8726	1.7388	1.2216
0.7	−1.2203	−0.8641	1.7084	1.2097
0.8	−1.1995	−0.8559	1.6793	1.1983
0.9	−1.1798	−0.8480	1.6517	1.1872
1.0	−1.1609	−0.8404	1.6253	1.1766

The NN permits the inverse relation with varied heat conductivity for both surfaces. It is significant to notice that the Nusselt number's strength is higher for flat surfaces than for cylindrical surfaces. At the plate and cylinder, the effect of the Prandtl number on the NN is explored (see Table 5). It is obvious that the NN displays levels of stimulation for higher Prandtl numbers. When the influence of heat generation is taken into account, the effect of the Prandtl number on NN is explored (see Table 6). We have seen, the NN rises as the Prandtl number does for both plates and cylinders. Both plate and cylindrical surfaces are considered in the evaluation of the Casson fluid parameter's impact on the Nusselt number. About the scenario of heat generation, Table 7 is provided. We found that the Nusselt number declines normally when Casson fluid parameter values increase. Moreover, cylindrical surfaces have a somewhat greater Nusselt number magnitude.

In Table 8, the NN at both surfaces are analyzed in relation to the Casson fluid parameter for the case when heat generation has no impact. We found that heat transfer normal to the surface tends to incline for larger Casson fluid parameter values.

Table 5. Impact of $\boldsymbol{Pr}$ on NN.

	$\boldsymbol{\theta_n'(0)}$		$\boldsymbol{-(1+4/3R_p)}$	
$\boldsymbol{Pr}$	$\gamma_p = 0$ (Plate)	$\gamma_p = 0.5$(Cylinder)	$\gamma_p = 0$ (Plate)	$\gamma_p = 0.5$ (Cylinder)
0.7	−0.4278	−0.5235	0.5989	0.7329
0.8	−0.4588	−0.5283	0.6423	0.7396
0.9	−0.4879	−0.5333	0.6831	0.7466
1.0	−0.5152	−0.5385	0.7213	0.7539
2.0	−0.5652	−0.5492	0.7913	0.7689
3.0	−0.6114	−0.5601	0.8560	0.7841
4.0	−0.6537	−0.5708	0.9152	0.7991
5.0	−0.6931	−0.5815	0.9703	0.8141
6.0	−0.7301	−0.5914	1.0221	0.8280
7.0	−0.8893	−0.6333	1.245	0.8866

Table 6. Impact of $\boldsymbol{Pr}$on NN when $H_p = 0$.

	$\boldsymbol{\theta_n'(0)}$		$\boldsymbol{-(1+4/3R_p)}$	
$\boldsymbol{Pr}$	$\gamma_p = 0$ (Plate)	$\gamma_p = 0.5$(Cylinder)	$\gamma_p = 0$ (Plate)	$\gamma_p = 0.5$ (Cylinder)
0.7	−0.4356	−0.5686	0.6098	0.7960
0.8	−0.4669	−0.5781	0.6537	0.8093
0.9	−0.4964	−0.5875	0.6950	0.8225
1.0	−0.5242	−0.5969	0.7339	0.8357
2.0	−0.7450	−0.6839	1.0430	0.9575
3.0	−0.9102	−0.7546	1.2743	1.0564
4.0	−1.0471	−0.8102	1.4659	1.1343
5.0	−1.1662	−0.8547	1.6327	1.1966
6.0	−1.2728	−0.8911	1.7819	1.2475
7.0	−1.3699	−0.9213	1.9179	1.2898

Table 7. Impact of β_p on NN [26].

	$\boldsymbol{\theta_n'(0)}$		$\boldsymbol{-(1+4/3R_p)}$	
$\boldsymbol{\beta_p}$	$\gamma_p = 0$ (Plate)	$\gamma_p = 0.5$(Cylinder)	$\gamma_p = 0$ (Plate)	$\gamma_p = 0.5$ (Cylinder)
0.1	−0.4052	−0.6093	0.5673	0.8530
0.2	−0.3953	−0.6095	0.5534	0.8533
0.3	−0.3911	−0.6089	0.5475	0.8525
0.4	−0.3888	−0.6085	0.5443	0.8519
0.5	−0.3863	−0.6082	0.5408	0.8515
0.6	−0.3855	−0.6080	0.5397	0.8512
0.7	−0.3850	−0.6078	0.5390	0.8509
0.8	−0.3845	−0.6077	0.5383	0.8508
0.9	−0.3840	−0.6076	0.5376	0.8506
1.0	−0.3838	−0.6075	0.5373	0.8505

Table 8. Impact of β_p on NN when $H_p = 0$ [26].

	$\boldsymbol{\theta_n'(0)}$		$\boldsymbol{-(1+4/3R_p)}$	
$\boldsymbol{\beta_p}$	$\gamma_p = 0$ (Plate)	$\gamma_p = 0.5$(Cylinder)	$\gamma_p = 0$ (Plate)	$\gamma_p = 0.5$ (Cylinder)
0.1	−0.2982	−0.2125	0.4175	0.2975
0.2	−0.3281	−0.4017	0.4593	0.5624
0.3	−0.3412	−0.4635	0.4777	0.6489
0.4	−0.3489	−0.4940	0.4885	0.6916
0.5	−0.3534	−0.5120	0.4948	0.7168
0.6	−0.3562	−0.5238	0.4987	0.7333
0.7	−0.3582	−0.5283	0.5015	0.7396
0.8	−0.3592	−0.5384	0.5029	0.7538
0.9	−0.3605	−0.5432	0.5047	0.7605
1.0	−0.4250	−0.5470	0.5950	0.7658

Table 9 shows how the thermal radiation parameter affects the NN. NN increases as thermal radiation strength does. Also, in the case of cylindrical surfaces, the NN is larger. When the heat generation effect is absent, Table 10 shows how the thermal radiation parameter affects the NN at both surfaces. For both frames, we saw that greater radiation parameter values lead to larger NN values. It is significant to notice that in the case of flat plates, the Nusselt number strength is higher. Our interest is to predict the values of the NN by using ANN models. For the prediction of the Nusselt number at both surfaces, we have built two separate ANN models (NN-ANN-I and NN-ANN-II). At a flat surface, NN-ANN-I owns the Nusselt number values, whereas NN-ANN-II owns the Nusselt number values at a cylindrical surface. One crucial step in the development of an ANN model is network training. The network was trained using the Levenberg-Marquardt method. Figures 2 and 3 show the training results for NN-ANN models. Specifically, Figure 2 presents the training of the ANN model for the forecast of NN at a flat surface, whereas Figure 3 for the prediction of NN at a cylindrical surface. For NN-ANN-I, the finest validation (FV) is 0.029329 at epoch 5 and for NN-ANN-II, the FV is 0.0.0099961 at epoch 29. We noticed that the MSE values for both graphs start out high and then start to decline as the stages go-on. The error histogram (EH) of the NN-ANN models being built to forecast Nusselt number values is shown in Figures 4 and 5. The EH of model-I is shown in Figure 4, whereas the EH of the model-II for a cylindrical surface is shown in Figure 5. The EHs in both cases have 20 Bins.

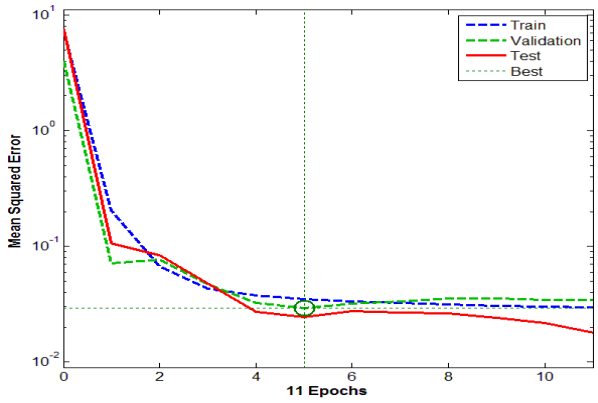

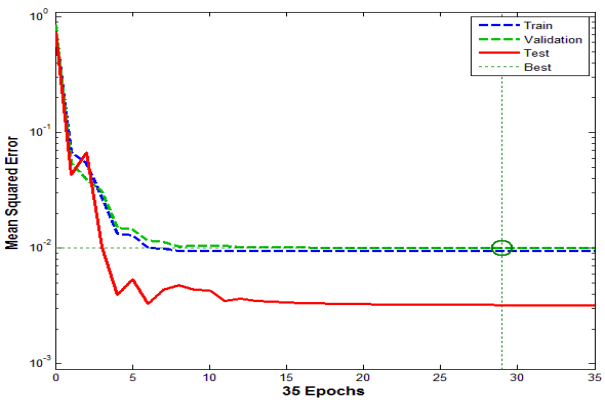

Figure 2. ANN model-I training performance graph. **Figure 3.** ANN model-II training performance graph.

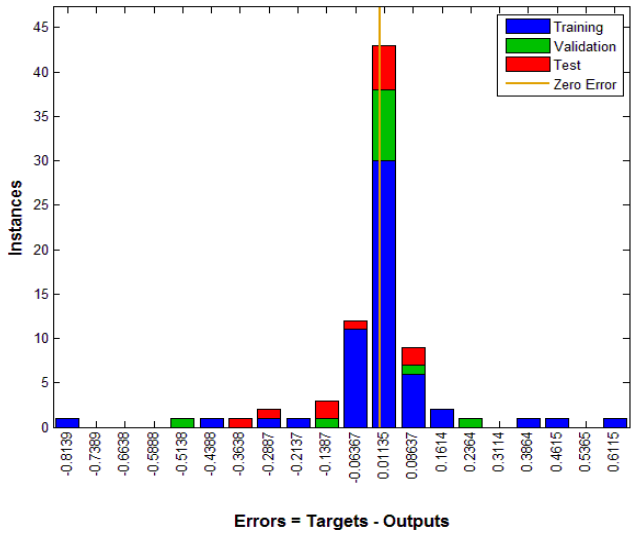

Figure 4. ANN model-I error histogram.

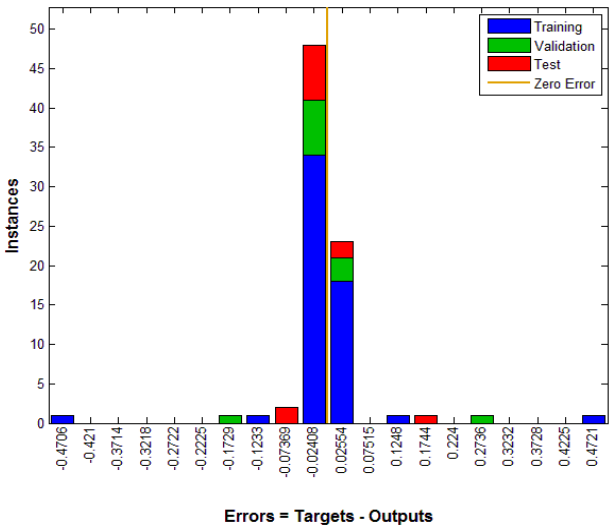

Figure 5. ANN model-II error histogram.

Table 9. Impact of R_p on NN [26].

	$\boldsymbol{\theta_n'(0)}$		$\boldsymbol{-(1+4/3R_p)}$	
$\boldsymbol{R_p}$	$\gamma_p = 0$ (Plate)	$\gamma_p = 0.5$(Cylinder)	$\gamma_p = 0$ (Plate)	$\gamma_p = 0.5$ (Cylinder)
0.1	−0.5235	−0.4278	0.5933	0.4848
0.2	−0.5215	−0.4058	0.6605	0.5140
0.3	−0.5200	−0.3868	0.7280	0.5415
0.4	−0.5188	−0.3703	0.7954	0.5678
0.5	−0.5179	−0.3557	0.8631	0.5929
0.6	−0.5171	−0.3428	0.9308	0.6170
0.7	−0.5166	−0.3314	0.9988	0.6407
0.8	−0.5161	−0.3212	1.0667	0.6638
0.9	−0.5157	−0.3121	1.1345	0.6867
1.0	−0.5154	−0.3038	1.2026	0.7089

Table 10. Impact of $\boldsymbol{R_p}$ on NN when $H_p = 0$.

	$\boldsymbol{\theta_n'(0)}$		$\boldsymbol{-(1+4/3R_p)}$	
$\boldsymbol{R_p}$	$\gamma_p = 0$ (Plate)	$\gamma_p = 0.5$(Cylinder)	$\gamma_p = 0$ (Plate)	$\gamma_p = 0.5$ (Cylinder)
0.1	−1.4994	−0.9564	1.6993	1.0839
0.2	−1.4302	−0.9383	1.8116	1.1885
0.3	−1.3699	−0.9213	1.9179	1.2898
0.4	−1.3167	−0.9054	2.0189	1.3883
0.5	−1.2693	−0.8905	2.1155	1.4842
0.6	−1.2267	−0.8765	2.2081	1.5777
0.7	−1.1882	−0.8633	2.2972	1.669
0.8	−1.1530	−0.8509	2.3829	1.7585
0.9	−1.1208	−0.8392	2.4658	1.8462
1.0	−1.0912	−0.8281	2.5461	1.9322

Since both NN-ANN models' error values are quite low, the training stages of NN-ANN-I and NN-ANN-II to estimate Nusselt numbers at both surfaces are successfully finished. The mean square error graphs for the Nusselt number are shown in Figures 6 and 7. Here, Figure 6 shows the MSE for the NN at the plat surface, and Figure 7 shows the MSE for the NN at cylinder. Both figures show that NN-ANN-I and NN-ANN-II have successfully completed their learning stages. For use of 80 data samples, the MSE values are displayed. The MSE values' proximity to zero indicates that the NN-ANN models were trained with fewer mistakes to predict the Nusselt number. While MSE is recorded as 0.03261 for flat surface, and the average MSE for cylindrical surfaces is 0.008562777. The regression outcomes of Nusselt number data for both surfaces are given in Figures 8 and 9. It is key to remember that the regression value provides a correlation between the objectives and forecasts values; if this value is near to one (1), we can state there is a close link.

The developed NN-ANN-I and NN-ANN-II are the best models to forecast the NN at both surfaces, according to Figures 8 and 9.

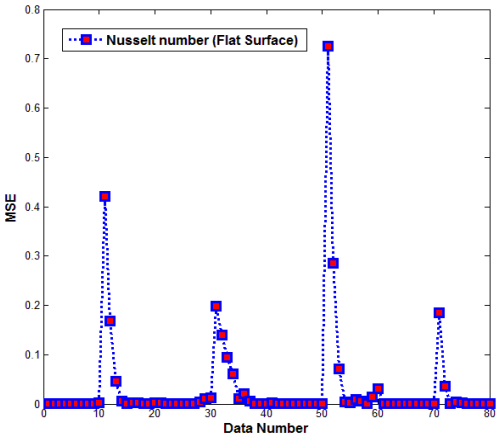

Figure 6. MSE for NN at plate.

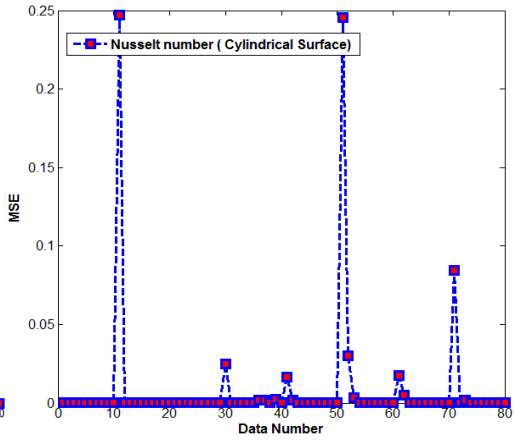

Figure 7. MSE for NN at cylinder.

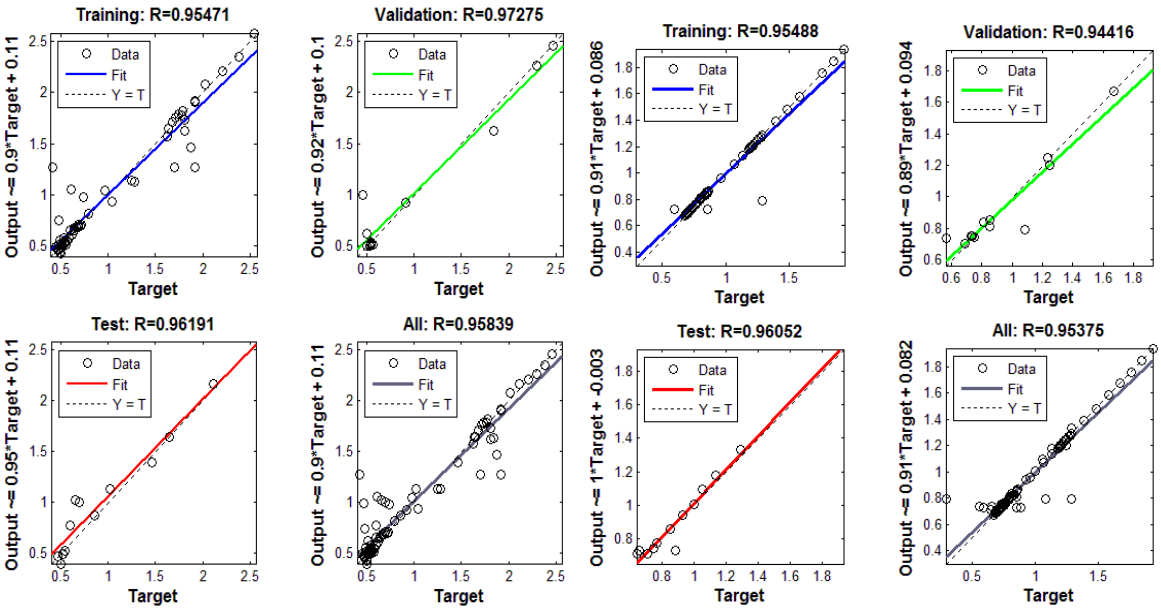

Figure 8. Values of regression for the ANN model I. **Figure 9.** Values of regression for the ANN model II.

Figures 10 and 11 compare the Nusselt number's actual values with those predicted by an artificial neural networking model. Figure 10 compares NN-ANN and the target data set for plate whereas Figure 11 compares NN-ANN and the target data set for cylinder. We can note from figures that the bulk of NN-ANN model outputs is in good agreement with the Nusselt number target values. Due to this overlap, we may conclude that the generated models, NN-ANN-I and NN-ANN-II, are highly accurate in predicting Nusselt numbers.

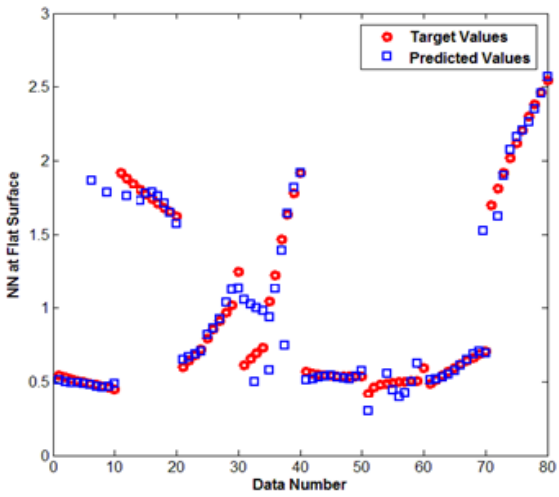

Figure 10. Result comparison for ANN-I.

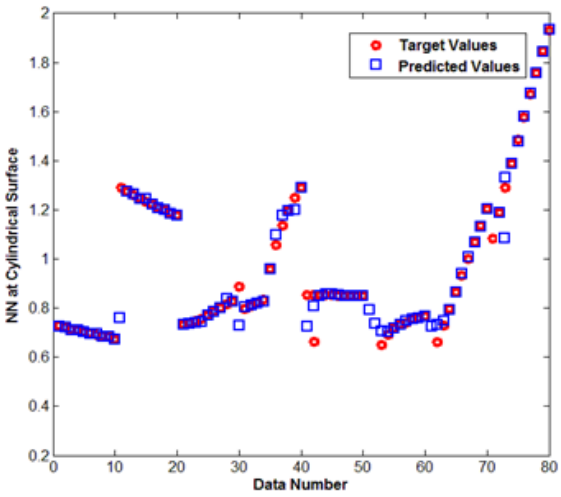

Figure 11. Result comparison for ANN-II.

The effect of a positive modification in the H_p on temperature is shown in Figures 12 and 13. Figure 12 shows the impact of heat generation on temperature for a plate, while Figure 13 shows the impact of heat generation on temperature for a cylindrical surface. It can be demonstrated that the temperature of the Casson fluid and the heat generation parameter are directly related. Positive values of the H_p cause energy generation, which raises the temperature. The effect of the Pr on the temperature is seen in Figures 14 and 15. In more detail, Figures 14 and 15 show how the Prandt number affects the temperature of a fluid over a flat surface and a cylindrical surface, respectively. We have seen that the Prandt number enables an indirect relation to Casson fluid temperature.

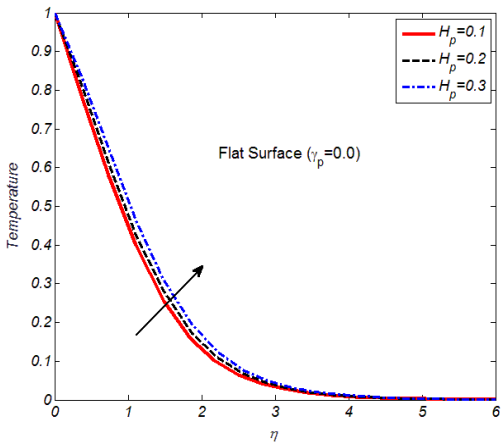

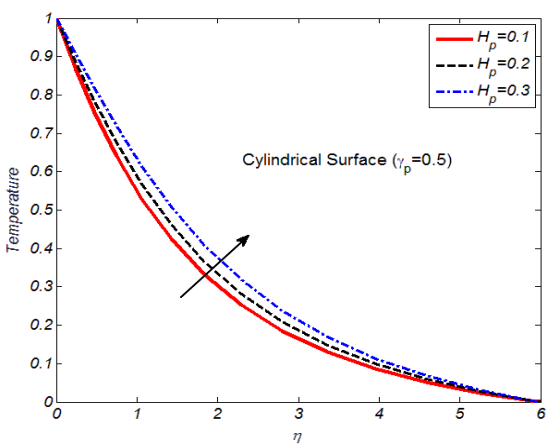

Figure 12. Effect of H_p on temperature at flat surface. **Figure 13**. Effect of H_p on temperature at cylindrical surface.

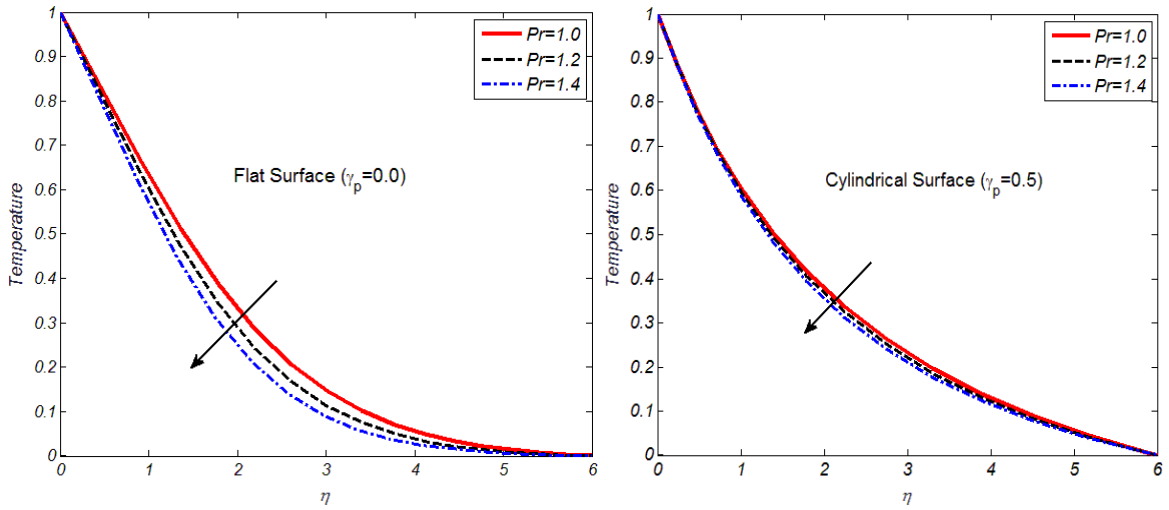

Figure 14. Effect of Pr on temperature at flat surface. **Figure 15.** Effect of Pr on temperature at cylindrical surface.

As the Prandtl number admits an inverse relationship to thermal conductivity, larger Prandtl number values result in a decrease in thermal conductivity. The fluid temperature drops as a result. For both flat and cylindrical surfaces, the effect of varying thermal conductivity on Casson fluid temperature is examined. Figures 16 and 17 provide evidence in this regard. Figure 16 describes the effect of variable thermal conductivity on the temperature in more detail, and we found that temperature rises as the ε_T rises. Similar to Figure 16, Figure 17 demonstrates how ε_T affects temperature over a cylinder. We found that fluid temperature exhibits tendencies that are indicative of variations in ε_T. Table 11 provides performance details for both ANN models, and it is clear that the constructed models are capable of accurately forecasting the values of the heat transfer coefficient at both flat and cylindrical surfaces.

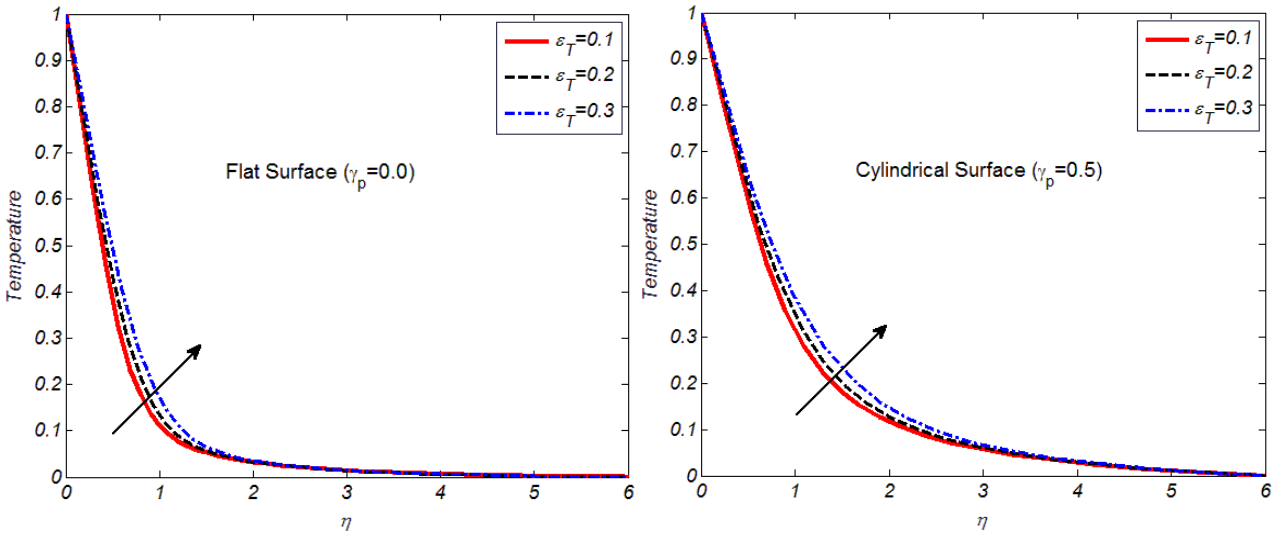

Figure 16. Effect of ε_T on temperature at flat surface. **Figure 17.** Effect of ε_T on temperature at cylindrical surface.

Table 11. Grades of NN-ANN models.

		MSE			R		
Model	Surface	Training	Validation	Test	Training	Validation	Test
NN-Model-I	$(\gamma_{p=}0.0)$	0.0350	0.0293	0.0246	0.9547	0.9727	0.9619
NN-Model-II	$(\gamma_{p=}0.5)$	0.0094	0.0100	0.0032	0.9549	0.9442	0.9605

6. Conclusions

Thermally magnetized Casson stagnation flow over an inclined surfaces is studied numerically. Mixed convection, thermal radiations, heat generation, viscous dissipation, and temperature-dependent thermal conductivity all contribute to the flow. Using artificial neural networking models, the NN is evaluated at both surfaces toward five various flow factors. The following are the key outcomes:

- For an inclined cylindrical surface, an average Mean Square Error (MSE) is recorded as 0.008562777 while for a flat surface it is recorded as 0.03261.
- The values of the coefficient of determination suggest artificial neural networks as the best method for predicting the NN at both surfaces.
- For both surfaces, the temperature admits direct relation for heat generation and thermal conductivity parameters.
- For higher Prandtl number, the Casson fluid temperature shows decline values. The such trend holds for both surfaces.
- According to the predictions made by NN-ANN models, we found that for cylindrical surface, the strength of the NN is greater than the flat surface.
- The Nusselt number admits indirect relation for variable thermal conductivity, and Casson parameters while the opposite is the case for thermal radiation parameter and Prandtl number.
- A neural networking approach can be used to predict the surface quantities being involved for the fluid flow over non-linear stretched surfaces having engineering standpoints.

Acknowledgments

The authors would like to thank Prince Sultan University, Saudi Arabia, for the technical support through the TAS research lab. Author (Haitham M. S. Bahaidara) is thankful for the financial support provided by the Interdisciplinary Research Center for Renewable Energy and Power Systems, King Fahd University of Petroleum and Minerals, for funding this research through Project no: INRE2212.

Conflict of interest

The authors declare no conflict of interest.

References

1. M. A. Dweib, C. M. ÓBrádaigh, Extensional and shearing flow of a glass-mat-reinforced thermoplastics (GMT) material as a non-Newtonian viscous fluid, *Compos. Sci. Technol.,* **59** (1999), 1399–1410. https://doi.org/10.1016/S0266-3538(98)00182-1

2. K. A. Fisher, R. J. Wakeman, T. W. Chiu, O. F. J. Meuric. Numerical modelling of cake formation and fluid loss from non-Newtonian muds during drilling using eccentric/concentric drill strings with/without rotation, *Chem. Eng. Res. Design*, **78** (2000), 707–714. https://doi.org/10.1205/026387600527888
3. Y. A. Berezin, V. A. Chugunov, K. Hutter, Hydraulic jumps on shallow layers of non-Newtonian fluids, *J. Non-newtonian Fluid Mech.,* **101** (2001), 139–148. https://doi.org/10.1016/S0377-0257(01)00154-9
4. H. Z. Li, Y. Mouline, N. Midoux, Modelling the bubble formation dynamics in non-Newtonian fluids, *Chem. Eng. Sci.,* **57** (2002), 339–346. https://doi.org/10.1016/S0009-2509(01)00394-3
5. M. Anand, K. R. Rajagopal, A shear-thinning viscoelastic fluid model for describing the flow of blood, *Int. J. Cardiovascular Medicine Sci.,* **4** (2004), 59–68. http://www.cs.cmu.edu/afs/cs.cmu.edu/project/taos-10/publications/MAKRR2004.pdf
6. Z. Yu, A. Wachs, Y. Peysson, Numerical simulation of particle sedimentation in shear-thinning fluids with a fictitious domain method, *J. Non-Newtonian Fluid Mech.,* **136** (2006), 126–139. https://doi.org/10.1016/j.jnnfm.2006.03.015
7. J. Marn, P. Ternik, Laminar flow of a shear-thickening fluid in a 90 pipe bend, *Fluid Dyn. Res..,* **38** (2006), 295. https://doi.org/10.1016/j.fluiddyn.2006.01.003
8. S. Guillou, R. Makhloufi, Effect of a shear-thickening rheological behaviour on the friction coefficient in a plane channel flow: A study by direct numerical simulation, *J. Non-Newtonian Fluid Mech.,* **144** (2007), 73–86. https://doi.org/10.1016/j.jnnfm.2007.03.008
9. S. U. Siddiqui, S. Mishra, A study of modified Casson's fluid in modelled normal and stenotic capillary-tissue diffusion phenomena, *Appl. Math. Comp.,* **189** (2007), 1048–1057. https://doi.org/10.1016/j.amc.2006.11.151
10. M. H. Abolbashari, N. Freidoonimehr, F. Nazari, M. M. Rashidi, Analytical modeling of entropy generation for Casson nano-fluid flow induced by a stretching surface, *Adv. Powder Tech.,* **26** (2015), 542–552. https://doi.org/10.1016/j.apt.2015.01.003
11. K. Bhattacharyya, M. S. Uddin, G. C. Layek, Exact solution for thermal boundary layer in Casson fluid flow over permeable shrinking sheet with variable wall temperature and thermal radiation, *Alex. Eng. J.,* **55** (2016), 1703–1712. https://doi.org/10.1016/j.aej.2016.03.010
12. M. Abd El-Aziz, A. S. Yahya, Perturbation analysis of unsteady boundary layer slip flow and heat transfer of Casson fluid past a vertical permeable plate with Hall current, *Appl. Math. Comput.,* **307** (2017), 146–164. https://doi.org/10.1016/j.amc.2017.02.034
13. M. Nawaz, R. Naz, M. Awais, Magnetohydrodynamic axisymmetric flow of Casson fluid with variable thermal conductivity and free stream, *Alex. Eng. J.,* **57** (2018), 2043–2050 https://doi.org/10.1016/j.aej.2017.05.016
14. M. Usman, F. A. Soomro, R. Ul Haq, W. Wang, O. Defterli, Thermal and velocity slip effects on Casson nanofluid flow over an inclined permeable stretching cylinder via collocation method, *Inter. J. Heat Mass Trans.,* **122** (2018), 1255–1263 https://doi.org/10.1016/j.ijheatmasstransfer.2018.02.045
15. A. Tassaddiq, I. Khan, K. S. Nisar, J. Singh, MHD flow of a generalized Casson fluid with Newtonian heating: A fractional model with Mittag–Leffler memory, *Alex. Eng. J.,* **59** (2020), 3049–3059. https://doi.org/10.1016/j.aej.2020.05.033
16. F. Hussain, M. Nazeer, M. Altanji, A. Saleem, M. M. Ghafar, Thermal analysis of Casson rheological fluid with gold nanoparticles under the impact of gravitational and magnetic forces, *Case Stud. Thermal Eng.,* **28** (2021), 101433. https://doi.org/10.1016/j.aej.2020.05.033

17. M. T. Akolade, Y. O. Tijani, A comparative study of three dimensional flow of Casson–Williamson nanofluids past a riga plate: Spectral quasi-linearization approach, *Part. Diff. Eqs. Appl. Math.,* **4** (2021), 100108. https://doi.org/10.1016/j.padiff.2021.100108
18. B. K. Siddiqui, S. Batool, M. Y. Malik, Q. Mahmood ul Hassan, Ali S. Alqahtani, Darcy Forchheimer bioconvection flow of Casson nanofluid due to a rotating and stretching disk together with thermal radiation and entropy generation, *Case Studies Thermal Eng.,* **27** (2021), 101201. https://doi.org/10.1016/j.csite.2021.101201
19. S. G. Bejawada, Y. D. Reddy, W. Jamshed, K. Sooppy Nisar, A. N. Alharbi, R. Chouikh. Radiation effect on MHD Casson fluid flow over an inclined non-linear surface with chemical reaction in a Forchheimer porous medium, *Alex. Eng. J.,* **61** (2022), 8207–8220. https://doi.org/10.1016/j.aej.2022.01.043
20. M. R. Khan, A. S. Al-Johani, A. MA Elsiddieg, T. Saeed, A. Mousa Abd Allah, The computational study of heat transfer and friction drag in an unsteady MHD radiated Casson fluid flow across a stretching/shrinking surface, *Int. Comm. Heat Mass Trans.,* **130** (2022), 105832. https://doi.org/10.1016/j.icheatmasstransfer.2021.105832
21. A. C. Venkata Ramudu, K. Anantha Kumar, V. Sugunamma, N. Sandeep, Impact of Soret and Dufour on MHD Casson fluid flow past a stretching surface with convective–diffusive conditions, *J. Therm. Anal. Calorim.,* **147** (2022), 1–11. https://doi.org/10.1007/s10973-021-10569-w
22. T. Hayat, S. A. Khan, S. Momani, Finite difference analysis for entropy optimized flow of Casson fluid with thermo diffusion and diffusion-thermo effects, *Inter. J. Hydrogen Ener.,* **47** (2022), 8048–8059. https://doi.org/10.1016/j.ijhydene.2021.12.093
23. M. Afrand, N. Sina, H. Teimouri, A. Mazaheri, M. R. Safaei, M. H. Esfe, et al., Effect of magnetic field on free convection in inclined cylindrical annulus containing molten potassium, *Inter. J. Appl. Mech.,***7** (2015), 1550052. https://doi.org/10.1142/S1758825115500520
24. M. S. Dehghani, D. Toghraie, B. Mehmandoust, Effect of MHD on the flow and heat transfer characteristics of nanofluid in a grooved channel with internal heat generation, *Inter. J. Num. Methods. Heat Fluid Flow.,* **29** (2018), 1403–1431. https://doi.org/10.1108/HFF-05-2018-0235
25. K. Ur, Rehman, M. Awais, A. Hussain, N. Kousar, M. Y. Malik, Mathematical analysis on MHD Prandtl-Eyring nanofluid new mass flux conditions, *Math. Method. Appl. Sci.,* **42** (2019), 24–38. https://doi.org/10.1002/mma.5319
26. K. Ur. Rehman, W. Shatanawi, S. Yaseen, A comparative numerical study of heat and mass transfer individualities in Casson stagnation point fluid flow past a flat and cylindrical surfaces, *Mathematics.,***11** (2023), 470. https://doi.org/10.3390/math11020470
27. K. Ur. Rehman, W. Shatanawi, U. Firdous, A comparative thermal case study on thermophysical aspects in thermally magnetized flow regime with variable thermal conductivity, *Case Stud. Therm. Eng.,* **44** (2023), 102839. https://doi.org/10.1016/j.csite.2023.102839
28. G. Tunc, Y. Bayazitoglu, Heat transfer in microtubes with viscous dissipation, *Inter. J. Heat Mass Trans.,* **44** (2001), 2395–2403. https://doi.org/10.1016/S0017-9310(00)00298-2
29. K. Ur. Rehman, Q. M. Al-Mdallal, M. Y. Malik, Symmetry analysis on thermally magnetized fluid flow regime with heat source/sink, *Case Stud. Therm. Eng.,* **14** (2019), 100452. https://doi.org/10.1016/j.csite.2019.100452

30. P. Barnoon, D. Toghraie, R. B. Dehkordi, H. Abed, MHD mixed convection and entropy generation in a lid-driven cavity with rotating cylinders filled by a nanofluid using two phase mixture model, *J. Magnet. Magnet. Material,* **483** (2019), 224–248. https://doi.org/10.1016/j.jmmm.2019.03.108
31. D. Toghraie, Numerical simulation on MHD mixed convection of Cu-water nanofluid in a trapezoidal lid-driven cavity, *Inter. J. Appl. Electrom.,* **62** (2020), 683–710. https://doi.org/10.3233/JAE-190123
32. H. Sadaf, Z. Asghar, N. Iftikhar, Cilia-driven flow analysis of cross fluid model in a horizontal channel, *Comp. Part. Mech.*, (2022), 1–8. https://doi.org/10.1007/s40571-022-00539-w
33. A. Aabid, S. Afghan Khan, M. Baig, Numerical analysis of a microjet-based method for active flow control in convergent-divergent nozzles with a sudden expansion duct, *Fluid Dynam. Mater. Process.,* **18** (2022), 1–24. https://doi.org/10.32604/fdmp.2022.021860
34. I. S. Hussain, D. Prakash, B. Abdalla, M. Muthtamilselvan, Analysis of Arrhenius activation energy and chemical reaction in nanofluid flow and heat transfer over a thin moving needle, *Current Nanosci.*, **19** (2023), 39–48. https://doi.org/10.2174/1573413717666211117150656
35. K. Ur Rehman, A. Batur Çolak, W. Shatanawi, Artificial neural networking (ANN) model for drag coefficient optimization for various obstacles, *Mathematics,* **10** (2022), 2450. https://doi.org/10.3390/math10142450
36. A. B. Çolak, An experimental study on the comparative analysis of the effect of the number of data on the error rates of artificial neural networks, *Int. J. Ener. Resear.,* **45** (2021), 478–500. https://doi.org/10.1002/er.5680
37. A. Shafiq, A. Batur Çolak, T. Naz Sindhu, Designing artificial neural network of nanoparticle diameter and solid–fluid interfacial layer on single-walled carbon nanotubes/ethylene glycol nanofluid flow on thin slendering needles, *Int. J. Num. Methods Fluids,* **93** (2021), 3384–3404. https://doi.org/10.1002/fld.5038
38. A. Shafiq, A. Batur Çolak, T. Naz Sindhu, Q. M. Al-Mdallal, T. Abdeljawad, Estimation of unsteady hydromagnetic Williamson fluid flow in a radiative surface through numerical and artificial neural network modeling, *Sci. Rep.,***11** (2021), 14509. https://doi.org/10.1038/s41598-021-93790-9
39. A. B. Colak, Experimental study for thermal conductivity of water-based zirconium oxide nanofluid: developing optimal artificial neural network and proposing new correlation, *Int. J. Energy Res.,* **45** (2021), 2912–2930. https://doi.org/10.1002/er.5988
40. M. Adamu, A. Batur Çolak, Y. E. Ibrahim, S. I. Haruna, M. F. Hamza, Prediction of mechanical properties of rubberized concrete incorporating fly ash and nano silica by artificial neural network technique, *Axiom.,* **12** (2023), 81. https://doi.org/10.3390/axioms12010081

AIMS Press